Mechanism behind qubit gates as interfering quantum pathway amplitudes

Michael Kasprzak,[1,*] Gaurav Bhole,[2] and Herschel Rabitz[1]

[1] *Princeton University*
[2] *Harvard University*

(Dated: February 9, 2024)

Hamiltonian encoding was introduced as a technique for revealing the mechanism of controlled quantum systems. It does so by decomposing the evolution into pathways between eigenstates, where each pathway has an associated complex amplitude. The magnitude of a pathway amplitude determines its significance and many pathways constructively and destructively interfere to produce the final evolution of the system. In this paper, we apply the Hamiltonian encoding technique to qubit gates implemented via control pulses. The mechanism by which these pulses operate is given by pathways between the computational basis states. An X gate, two CNOT gates, and a SWAP gate are examined to demonstrate the key ideas that different controls produce different mechanisms and efficiency is determined by the amount of interference.

I. INTRODUCTION

Creating a viable platform for quantum computing is an area of great interest and potential. Many different approaches have been suggested and each comes with different strategies for implementing qubits and implementing quantum gates on the system [1–6]. The implementation of quantum gates often involves the use of quantum optimal control to create external fields to manipulate a quantum system in order to achieve a specific goal [7–9]. In these cases, the goal is a unitary transformation corresponding to a quantum gate. Quantum optimal control has been repeatedly studied both theoretically [10–16] and experimentally [17–22] in many context. Particularly important to quantum computing implementation, quantum control has been extended to create robust controls that achieve high fidelities despite the presence of noise and errors [23–27].

Despite gate creation via optimal control being an active area of research, the mechanism behind how quantum gates are implemented has not been studied before. The pulses generated by optimal control algorithms are often complicated and there is little physical insight behind the quantum dynamics that are occurring. A definition of mechanism was proposed by Mitra and Rabitz that decomposed the evolution of a quantum system into a set of quantum pathways [28]. These quantum pathways each correspond to complex numbers known as pathway amplitudes which constructively and destructively interfere to produce the dynamics of a quantum system. These pathways and pathway amplitudes provide a systemic and quantitative way of understanding what occurs during a control pulse. Additionally, Mitra and Rabitz proposed an efficient way of calculating pathway amplitudes known as Hamiltonian encoding [28] which has recently been further improved upon [29]. Pathway mechanism analysis has been applied to a variety of problems both in simulations [30–34] and experiments [35–37] and this paper extends that work to study the mechanism behind quantum gates. All work described in this paper was performed by numerical simulations. All systems in this paper model small numbers of qubits and were taken to be closed and noiseless. This paper provides several examples of pathway mechanism analysis being applied to demonstrate the physical insights that can be gleaned.

The background behind mechanistic quantum pathways and Hamiltonian encoding are provided in Section II. Section III provides the mechanism analysis of a single qubit X-gate, two CNOT gates, and a SWAP gate. It should be stated that other gates were examined in preparation of this work but those depicted here were chosen as representatives of the type of information that may be gained. Finally, concluding remarks and potential future applications are discussed in Section IV.

II. MECHANISTIC QUANTUM PATHWAYS AND HAMILTONIAN ENCODING

This section serves to review previous work as background on extracting mechanistic pathways via Hamiltonian encoding [28]. A quantum pathway between two states $|a\rangle$ and $|b\rangle$ is a sequence of states $|l_1\rangle, \ldots, |l_{n-1}\rangle$ connecting the two: $a \to l_1 \to \ldots \to l_{n-1} \to b$. The corresponding complex pathway amplitudes are obtained by interpreting terms in the Dyson series. Hamiltonian encoding is a procedure to calculate pathway amplitudes by modulating the Hamiltonian and decoding subsequent evolution instead of direct computation. More details on the theory behind quantum pathways and Hamiltonian encoding can be found at [28, 30, 32], and further details on computation and implementation can be found at [29].

A. Pathways in the Dyson Series

The n-qubit quantum systems addressed in this paper will be closed and noiseless. The general Hamiltonians for

* mk7592@princeton.edu

such systems can be written as $H(t) = H_0 + H_c(t)$ where H_0 is a constant drift term and $H_c(t)$ is a time-varying control term. The 2^n elements of the computational basis $|i\rangle$ are the eigenstates of the drift term $H_0 |i\rangle = E_i |i\rangle$ for $i = 0\cdots0, \ldots, 1\cdots1$.

To define a quantum pathway amplitude, we must switch to the interaction picture. Let $V(t) = \exp(iH_0t/\hbar)H_c(t)\exp(-iH_0t/\hbar)$ be defined as the interaction Hamiltonian. Then the Schrödinger equation is written as

$$i\hbar\frac{\mathrm{d}}{\mathrm{d}t}U(t) = V(t)U(t),\ U(0) = I \tag{1}$$

where $U(t)$ is the time evolution operator. The formal solution for $U(T)$ is given by the Dyson series:

$$\begin{aligned} U(T) = I &+ \left(\frac{-i}{\hbar}\right)\int_0^T V(t_1)\,\mathrm{d}t_1 \\ &+ \left(\frac{-i}{\hbar}\right)^2\int_0^T\int_0^{t_2} V(t_2)V(t_1)\,\mathrm{d}t_1\,\mathrm{d}t_2 \\ &+ \left(\frac{-i}{\hbar}\right)^3\int_0^T\int_0^{t_3}\int_0^{t_2} V(t_3)V(t_2)V(t_1)\,\mathrm{d}t_1\,\mathrm{d}t_2\,\mathrm{d}t_3 \\ &+ \cdots . \end{aligned} \tag{2}$$

If we insert the identity $I = \sum_{i=0}^{2^n-1}|i\rangle\langle i|$ between every matrix product and adopt the notations $U_{ba} = \langle b|U(T)|a\rangle$ and $v_{ji}(t) = -\frac{i}{\hbar}\langle j|V(t)|i\rangle$, then Eq. 2 can be expressed as

$$U_{ba} = \sum_{n=0}^{\infty}\sum_{l_{n-1}=0}^{2^n-1}\cdots\sum_{l_1=0}^{2^n-1} U_{ba}^{n(l_1,\ldots,l_{n-1})} \tag{3}$$

where

$$\begin{aligned} &U_{ba}^{n(l_1,\ldots,l_{n-1})} \\ &\equiv \int_0^T\int_0^{t_n}\cdots\int_0^{t_2} v_{bl_{n-1}}(t_n)v_{l_{n-1}l_{n-2}}(t_{n-1})\cdots \\ &\qquad\qquad v_{l_1a}(t_1)\,\mathrm{d}t_1\cdots\mathrm{d}t_{n-1}\,\mathrm{d}t_n\,. \end{aligned} \tag{4}$$

The index n in Eqs. 3 and 4 denotes the *order* of the term, i.e. the number of transitions induced by the interaction V. The parenthesis $(l_1,\ldots,l_{n-1})$ list $n-1$ intermediate states. An n-th order *pathway* between two states $|a\rangle$ and $|b\rangle$ is a sequence of n transitions $a\to l_1\to\ldots\to l_{n-1}\to b$ through $n-1$ intermediate states $|l_i\rangle$. Eq. 4 gives the complex *pathways amplitude* for a given pathway. Pathway amplitudes with larger magnitudes have larger contributions to the dynamics and phases allow various pathways to constructively and destructively interfere. For a given control problem there may be infinitely many pathways, but the core mechanism is determined by those with the largest amplitudes and the interference pattern between them.

In later analyses, it will be useful to group pathways with similar attributes into *pathway classes*. The amplitude of a pathway class is the sum of all the individual pathway amplitudes within the class. The two examples of pathways classes used in this paper will be Hermitian and non-Hermitian pathway classes. A *non-Hermitian pathway class*, denoted with an NH superscript, is a set of pathways that only differ by *time-sequencing*: the order in which transitions occur in a pathway. For example, the pathways $00\to01\to00\to10\to00$ and $00\to10\to00\to01\to00$ belong to the same non-Hermitian pathway class $[00\to01\to00\to10\to00]^{NH}$. Most non-Hermitian pathway classes like $[00\to01\to11]^{NH}$ only contain one pathway. A *Hermitian pathway class*, denoted with an H superscript, denotes the set of pathways that differ only by time-sequencing and *backtracking*. Backtracking is when a pathway includes a transition from state $|i\rangle$ to $|j\rangle$ and later a transition from $|j\rangle$ to $|i\rangle$. Backtracking includes Rabi flopping, which is when a pathway includes a transition from $|i\rangle$ to $|j\rangle$ and immediately thereafter a transition from $|j\rangle$ back to $|i\rangle$. For example, both $00\to10$ and $00\to01\to00\to10$ are members of the $[00\to10]^H$ Hermitian pathway class. Hermitian pathway classes do not provide as much information as the non-Hermitian case but are instead more useful in providing a more coarse-grain description of the mechanism.

B. Hamiltonian Encoding

In principle, each pathway amplitude $U_{ba}^{n(l_1,\ldots,l_{n-1})}$ may be computed directly via Eq. 4, but this becomes infeasible as the order n increases: the number of possible pathways grows exponentially due to the growing number of intermediate states $(l_1,\ldots,l_{n-1})$. Instead of directly computing these integrals, Hamiltonian encoding modulates the Hamiltonian in an additional time-like variable s and decodes the evolution of the subsequent modulated system to efficiently extract pathway amplitudes.

Hamiltonian encoding is most commonly implemented as *Fourier encoding*. This is when the Hamiltonian is modulated by multiplying each matrix element by a complex exponential

$$v_{ji}(t) \to v_{ji}(t;s) = e^{i\gamma_{ji}s}v_{ji}(t) \tag{5}$$

where each element was assigned a frequency γ_{ji}. This encoding gives the modulated Schroödinger equation:

$$\frac{\mathrm{d}U(t;s)}{\mathrm{d}t} = \begin{pmatrix} e^{i\gamma_{11}s}v_{11}(t) & \cdots & e^{i\gamma_{1d}s}v_{1d}(t) \\ \vdots & \ddots & \vdots \\ e^{i\gamma_{d1}s}v_{d1}(t) & \cdots & e^{i\gamma_{dd}s}v_{dd}(t) \end{pmatrix} U(t;s). \tag{6}$$

The modulated pathway amplitude $U_{ba}^{n(l_1,\ldots,l_{n-1})}(s)$ for a pathway $a\to l_1\to\ldots\to l_{n-1}\to b$ can be written as

$$\begin{aligned} &U_{ba}^{n(l_1,\ldots,l_{n-1})}(s) \\ &= \int_0^T\int_0^{t_n}\cdots\int_0^{t_2} v_{bl_{n-1}}(t_n)e^{i\gamma_{bl_{n-1}}s}\cdots \\ &\qquad\qquad v_{l_1a}(t_1)e^{i\gamma_{l_1a}s}\,\mathrm{d}t_1\cdots\mathrm{d}t_{n-1}\,\mathrm{d}t_n \\ &= U_{ba}^{n(l_1,\ldots,l_{n-1})}\,e^{i\gamma_{ba}^{n(l_1,\ldots,l_{n-1})}s} \end{aligned} \tag{7}$$

where

$$\gamma_{ba}^{n(l_1,\ldots,l_{n-1})} \equiv \gamma_{bl_{n-1}} + \cdots + \gamma_{l_1 a}. \tag{8}$$

Each pathway has an associated frequency $\gamma_{ba}^{n(l_1,\ldots,l_{n-1})}$. Akin to Eq. 3, the transition amplitude between $|a\rangle$ and $|b\rangle$ at final time T can be written as

$$U_{ba}(s) = \sum_{\text{pathways}} U_{ba}^{n(l_1,\ldots,l_{n-1})} \cdot e^{i\gamma_{ba}^{n(l_1,\ldots,l_{n-1})} s}. \tag{9}$$

This is a sum of complex sinusoidal terms each with a complex amplitude. Given sufficiently many sample points s, a Fourier transform can be used to efficiently extract the pathway amplitudes $U_{ba}^{n(l_1,\ldots,l_{n-1})}$ for a given frequency $\gamma_{ba}^{n(l_1,\ldots,l_{n-1})}$. The main computational cost of Hamiltonian encoding is solving Eq. 6 for different s-points. This procedure is laid out diagrammatically in Figure 1.

The choice of frequencies in Eq. 5 plays an important role in determining the mechanism obtained from Hamiltonian Encoding. Certain choices can give amplitudes corresponding to Hermitian and non-Hermitian pathways classes as defined in Section II A. *Hermitian encoding* is defined to be

$$\begin{gathered} v_{ji}(t) \to v_{ji}(t) e^{i\gamma_{ji} s} \\ \gamma_{ij} = -\gamma_{ji}. \end{gathered} \tag{10}$$

Using the constraint from above, pathways that contain backtracking (i.e. a $i \to j$ and a $j \to i$ transition) have frequencies that cancel in Eq. 8. All pathways that differ by only backtracking have the same pathway frequency $\gamma_{ba}^{n(l_1,\ldots,l_{n-1})}$. Therefore, the associated amplitude for this frequency is exactly the Hermitian pathway class amplitude: the sum of all constituent pathway amplitudes. Hermitian pathway classes are called as such since the encoding in Eq. 10 keeps the modulated Hamiltonian hermitian.

Non-Hermitian pathway class amplitudes are calculated using *non-Hermitian encoding* which relaxes the second condition in Eq. 10:

$$\begin{gathered} v_{ji} \to v_{ji} e^{i\gamma_{ji} s} \\ \gamma_{ij} \neq -\gamma_{ji}. \end{gathered} \tag{11}$$

Since the associated frequencies for $i \to j$ and $j \to i$ do not cancel, pathways that differ by backtracking will have different frequencies and therefore have distinguishable pathway amplitudes. Since the sum in Eq. 8 is commutative, non-Hermitian encoding has no way to distinguish time-sequencing information.

In both Hermitian and non-Hermitian encoding, there is still freedom regarding which values to assign to each individual γ_{ji}. Typically this is done to maximize the amount of pathway classes with unique associated frequencies. Additionally, recent work [29] has shown that not all transitions need to be modulated to determine a pathway from its frequency. This gives two new and more efficient encoding procedures to obtain Hermitian and non-Hermitian pathway classes, both of which were used in the computations in this paper. The reader is directed towards [29] for further details on picking frequencies and more efficient encodings.

III. MECHANISMS AND QUANTUM PATHWAYS BEHIND QUBIT GATES

In this section, mechanism analysis is applied to qubit systems to illustrate the important insights that can be gained by such techniques. The systems that we investigate are gates on either single or multi-qubit systems. Instead of looking at these gates as black-box operations, mechanism analysis looks at the fundamental quantum dynamics underlying a given control pulse. A precise, quantitative mechanism is given in terms of quantum pathways. Qubit systems are ideal for this view of mechanism because the computational basis states are a principal set of discrete states and pathways involve transitions between discrete states. This is as opposed to other regimes where quantum mechanics is more commonly looked at in a given set of coordinates. This paper serves to establish the foundational principles of pathway mechanism analysis in qubit systems. Discussion regarding further applications can be found in Section IV.

For the simulations performed in Sections III B and III C, Eq. 6 is solved numerically by approximating the control Hamiltonians as piecewise constant in time:

$$U(T;s) \approx \prod_{n=1}^{T/\Delta t} \exp\left(-\frac{i}{\hbar} V(n\Delta t; s)\Delta t\right). \tag{12}$$

When $V(n\Delta t; s)$ is Hermitian, the matrix exponential is efficiently calculated by diagonalizing V. When $V(n\Delta t; s)$ is not Hermitian (i.e. non-Hermitian encoding) the matrix exponential is computed using a squaring and scaling method [38]. OHPE and NHPE were used in the calculation of Hermitian and non-Hermitian pathway class amplitudes respectively [29].

A. X-Gate

The first system that will be looked at is a single qubit with an X-gate being applied. Working in the rotating frame, H_0 is set to $H_0 = 0$. An X-gate is implemented as an π-pulse, i.e.

$$H_c(t) = \begin{cases} \pi I_x & t < 1 \\ 0 & t > 1 \end{cases} \tag{13}$$

where I_x is the Pauli spin operator in the x direction. All analysis will be performed assuming that the system starts entirely in the $|0\rangle$ state, but the analysis starting in the $|1\rangle$ state is analogous. Population plots depicting the evolution of this system are depicted in Figure 2.

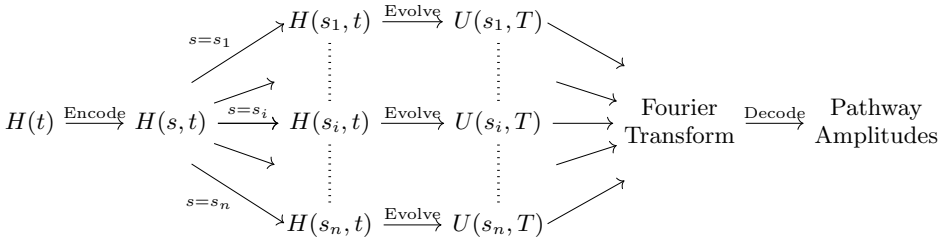

FIG. 1: A flowchart showing an outline of the Hamiltonian encoding process. The time-dependent Hamiltonian is modulated in a time-like parameter s. At many values of s, the modulated Schrödinger equation is solved via numerical integration to simulate the modulated system's evolution. The amplitudes of pathway classes are simultaneously extracted by decoding the evolution of these modulated systems via a Fourier transform.

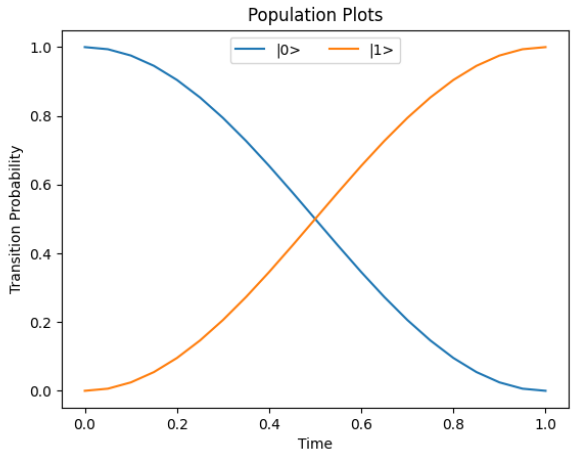

FIG. 2: Populations of the $|0\rangle$ and $|1\rangle$ states under the effect of a π-pulse with a Hamiltonian given by Eq. 13.

Pathway	Magnitude	Phase
0	1.000	0
$0\to1\to0$	1.234	180
$0\to1\to0\to1\to0$	0.254	0
$0\to1\to0\to1\to0\to1\to0$	0.021	180
...	...	...
Sum	0	180

Pathway	Magnitude	Phase
$0\to1$	1.571	270
$0\to1\to0\to1$	0.646	90
$0\to1\to0\to1\to0\to1$	0.080	270
$0\to1\to0\to1\to0\to1\to0\to1$	0.005	90
...	...	...
Sum	1.000	270

TABLE I: Pathways, amplitude magnitudes, and amplitude phases (in degrees) of the π-pulse on a two-level system. The overhead table includes pathways from $|0\rangle$ to $|0\rangle$ which perfectly destructively interfere since $U_{00}(T)=0$. The lower table includes pathways from $|0\rangle$ to $|1\rangle$ which perfectly interfere to get the desired $U_{10}(T)=1$ of a π-pulse.

This particular system is so simple that pathway amplitudes can be calculated analytically without the need for Hamiltonian encoding. Given a state $|0\rangle$ or $|1\rangle$, the only possible transition the system can make is to $|1\rangle$ or $|0\rangle$ respectively. Therefore, all pathways connecting $|0\rangle$ to $|0\rangle$ must have an even number of transitions with pathway amplitudes given by

$$U_{00}^n = \begin{cases} 0 & \text{n odd} \\ \frac{1}{n!}\left(\frac{-i\pi}{2}\right)^n & \text{n even} \end{cases} \tag{14}$$

where n is the order of the pathway. A similar results holds for pathways from $|0\rangle$ to $|1\rangle$:

$$U_{10}^n = \begin{cases} \frac{1}{n!}\left(\frac{-i\pi}{2}\right)^n & \text{n odd} \\ 0 & \text{n even} \end{cases}. \tag{15}$$

Pathways and their pathway amplitudes are calculated and depicted in Table I.

Figure 2 depicts a monotonically decreasing population in the $|0\rangle$ state and a monotonically increasing population in the $|1\rangle$ state. A first guess of the dominant pathways might have been only the $0\to1$ pathway, but Eq. 15 and Table I show the significance of higher order interactions in pathways. In reality, numerous pathways are oscillating back and forth between the $|0\rangle$ and $|1\rangle$ state at final time $T=1$ the 0 to 0 pathways perfectly destructively interfere to leave the whole system in the $|1\rangle$ state. The seemingly simple dynamics of a 2-level system are heavily dependent on higher-order interactions and interference patterns between pathway amplitudes. This mechanistic information was otherwise inaccessible.

B. CNOT Gate

In this section, two different implementations of a CNOT gate

$$\text{CNOT} = \begin{pmatrix} 1 & 0 & 0 & 0 \\ 0 & 1 & 0 & 0 \\ 0 & 0 & 0 & 1 \\ 0 & 0 & 1 & 0 \end{pmatrix} \tag{16}$$

are investigated to compare and contrast the differing mechanisms that achieve the same goal. The constant drift term of the full Hamiltonian is described by

$$H_0 = \omega_1(S_z \otimes \mathbb{I}) + \omega_2(\mathbb{I} \otimes S_z) + J(S_z \otimes S_z) \tag{17}$$

where S_z is the Pauli spin operator in the z direction, $\mathbb{I}$ is the 2×2 identity matrix, ω_1 and ω_2 are the resonance offset frequencies, and J are the J-coupling. The control term take the form of

$$H_c(t) = \epsilon_x(t)(S_x \otimes \mathbb{I} + \mathbb{I} \otimes S_x) + \epsilon_y(t)(S_y \otimes \mathbb{I} + \mathbb{I} \otimes S_y) \tag{18}$$

where S_x and S_y are the Pauli spin operators in the x and y directions and $\epsilon_x(t)$ and $\epsilon_x(t)$ are control fields being applied in the respective direction. The eigenstates of H_0 are the four two-qubit states: $|00\rangle$, $|01\rangle$, $|10\rangle$, and $|11\rangle$. The control Hamiltonian only allows for single qubit flips at a time, i.e. $00 \rightarrow 10$ and $11 \rightarrow 10$ are allowed but a transition like $00 \rightarrow 11$ is not. The two CNOT gates only differ in control fields $\epsilon_x(t)$ and $\epsilon_x(t)$ which were obtained by gradient ascent-based algorithms.

1. *First CNOT Gate*

The first CNOT gate that will be investigated has population plots shown in Figures 3 and 4. Although the basis consists of four states, only two population plots are depicted with the core difference that the control qubit is set to $|1\rangle$ in the second plot allowing the target qubit to change from $|0\rangle$ to $|1\rangle$. All of the following mechanism results are similar to the system starting in the $|01\rangle$ and $|11\rangle$ states, so they will not be discussed.

Before moving forward to the pathway mechanism, we discuss information that can be gleaned without the need for Hamiltonian encoding. The population plots in Figures 3 and 4 mainly show two states being present throughout the evolution in each case. When starting in $|00\rangle$, the control fields start flipping the target qubit, bringing the system in two $|01\rangle$ before undoing its progress in the second half of the pulse. In the second case starting in $|10\rangle$, the control fields flip the target qubit throughout the whole duration of the pulse, leaving the system entirely in the $|11\rangle$ state. The sinusoidal bumps in the populations are indications of Rabi-flopping, but no quantitative information can be made without Hamiltonian encoding. The control pulses are able to perform different actions on $|00\rangle$ and $|10\rangle$ because the $00 \rightarrow 01$ and $10 \rightarrow 11$ transitions have different resonant frequencies $\omega_{ij} = (E_i - E_j)/\hbar$.

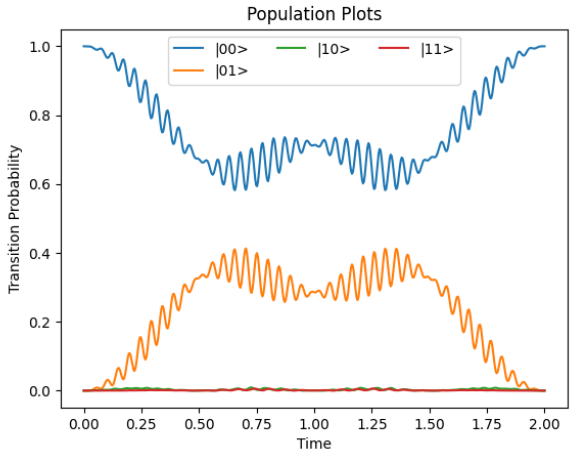

FIG. 3: Populations of all four computational basis states described by Eqs. 17 and 18 under the effect of the first CNOT gate acting on $|00\rangle$.

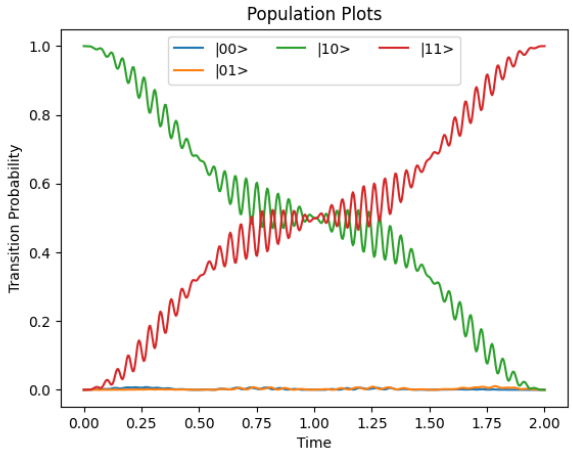

FIG. 4: Populations of all four computational basis states described by Eqs. 17 and 18 under the effect of the first CNOT gate acting on $|10\rangle$.

Non-Hermitian Hamiltonian encoding was performed on the system giving a set of non-Hermitian pathway classes and corresponding amplitudes. The choice of frequencies and encoding were performed according to the new algorithms in [29]. This four-dimensional system required only 16000 solves of Eq. 6. Tables II and III give the dominant pathways that evolved the system from $|00\rangle$ to $|00\rangle$ and $|10\rangle$ to $|11\rangle$ respectively. Since each pathway class corresponds to a complex pathway amplitude, these amplitudes can be plotted as arrows in the complex plane for easy visualization as is done in Figures 5 and 6.

Since non-Hermitian pathway classes do not hide backtracking information, they are optimal for quantitative information regarding the oscillations found in the pop-

$\gamma_{ba}^{n(l_1,\ldots,l_{n-1})}/\gamma_0$	Non-Hermitian Pathway Class	Magnitude	Phase
0	$[00]^{\mathrm{NH}}$	1.000	180.0
50	$[00\to10\to00]^{\mathrm{NH}}$	0.764	90.0
100	$[00\to10\to00\to10\to00]^{\mathrm{NH}}$	0.292	-1.0
57	$[00\to10\to00\to01\to00]^{\mathrm{NH}}$	0.181	-100.7
350	$[00\to01\to11\to01\to00]^{\mathrm{NH}}$	0.178	100.5
14	$[00\to01\to00\to01\to00]^{\mathrm{NH}}$	0.113	94.7
107	$[00\to10\to00\to10\to00\to01\to00]^{\mathrm{NH}}$	0.098	156.5
7	$[00\to01\to00]^{\mathrm{NH}}$	0.084	-86.7
...		...	...
Sum		1.000	135.0

TABLE II: Non-Hermitian pathway classes, amplitude magnitudes, and amplitude phases (in degrees) of the first CNOT gate driving the system from $|00\rangle$ to $|00\rangle$. All pathway classes with a magnitude greater than 0.083 are listed.

$\gamma_{ba}^{n(l_1,\ldots,l_{n-1})}/\gamma_0$	Non-Hermitian Pathway Class	Magnitude	Phase
0	$[10\to11]^{\mathrm{NH}}$	1.455	90.1
343	$[10\to11\to01\to11]^{\mathrm{NH}}$	0.631	-160.4
50	$[10\to00\to10\to11]^{\mathrm{NH}}$	0.586	161.5
2401	$[10\to11\to10\to11]^{\mathrm{NH}}$	0.355	-89.5
2744	$[10\to11\to10\to11\to01\to11]^{\mathrm{NH}}$	0.321	63.8
2451	$[10\to00\to10\to11\to10\to11]^{\mathrm{NH}}$	0.296	-60.6
686	$[10\to11\to01\to11\to01\to11]^{\mathrm{NH}}$	0.207	-63.9
100	$[10\to00\to10\to00\to10\to11]^{\mathrm{NH}}$	0.180	-112.0
4802	$[10\to11\to10\to11\to10\to11]^{\mathrm{NH}}$	0.149	-89.9
...		...	...
Sum		1.000	135.0

TABLE III: Non-Hermitian pathway classes, amplitude magnitudes, and amplitude phases (in degrees) of the first CNOT gate driving the system from $|10\rangle$ to $|11\rangle$. All pathway classes with a magnitude greater than 0.13 are listed.

ulation plots. Indeed, when looking at Tables II and III, if backtracking were removed, the pathways would all simplify to $00\to0$ or $10\to11$. The large amount of backtracking is not surprising given the sinusoidal bumps in the population plots and what was seen in the X-gate example in section III A: even the simplest systems exhibiting Rabi flopping. What is surprising is the states that the pathways used during backtracking. Specifically looking at the $10\to11$ case, there are many pathways (specifically the 2nd and 3rd most significant) in Table III with $|00\rangle$ and $|01\rangle$ as intermediate states. However, this is not what one would expect by looking at the population plot in Figure 4 where the $|00\rangle$ and $|01\rangle$ states have a low presence throughout the entirety of the time duration.

The reason why states can show up in pathways but not appear in the final population is due to destructive interference. Returning to the $10\to11$ example, consider the pathways with frequencies 343, 2744, and 686. All of these pathways as shown in Table III have $|01\rangle$ as an intermediate state. Identifying these pathways in the arrow plot in Figure 6 (the 686 pathway is unlabeled but points in the same direction as the 2451 pathway) reveals that they are all misaligned. Therefore they destructively interfere, leaving no $|01\rangle$ seen in the population plot. When combined with all the other pathway classes that do not use the $|01\rangle$ state, the sum of all the pathway amplitudes still gives a value with a magnitude near 1. Hence at the final time, the system will be entirely in the $|11\rangle$ state. This destructive interference of subsets of pathways allows for states to be important to the mechanism despite not physically showing up to the system.

2. *Second CNOT Gate*

The second CNOT gate being investigated acts on the same Hamiltonian system as the first, the only difference is a different set of control fields $\epsilon_x(t)$ and $\epsilon_y(t)$. Populations plots of the system starting in states $|00\rangle$ and $|10\rangle$ are depicted in Figures 7 and 8. The mechanism immediately seems more complicated. Both cases have significant populations in all four states at some point whereas in the previous case, two states stayed mostly dormant during the pulse. However in a similar manner to the first pulse, for the $|00\rangle$ state, the second half of the pulse seemingly undoes the evolution of the first half and for the $|10\rangle$ state, the second half of the pulse simply continues the evolution of the first.

It is unclear whether the underlying mechanism behind

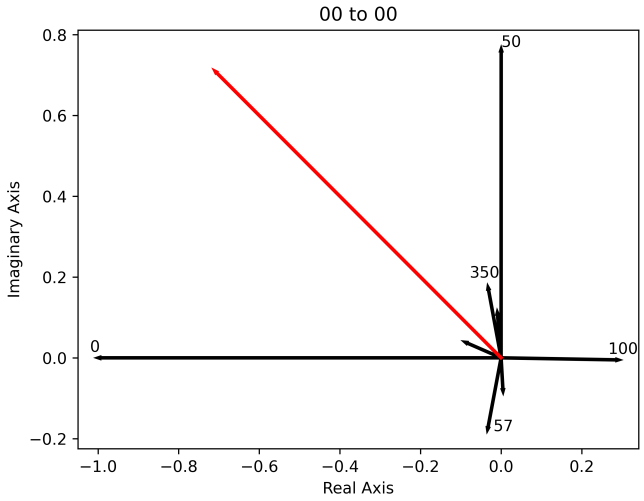

FIG. 5: The non-Hermitian pathway class amplitudes of the first CNOT gate for pathways from $|00\rangle$ to $|00\rangle$. Each amplitude is drawn as an arrow and pathway classes with large enough magnitudes are labeled with an associated frequency. The red arrow is the sum of all pathway class amplitudes and has a magnitude equal to 1. These non-Hermitian pathway classes are expanded in Table II.

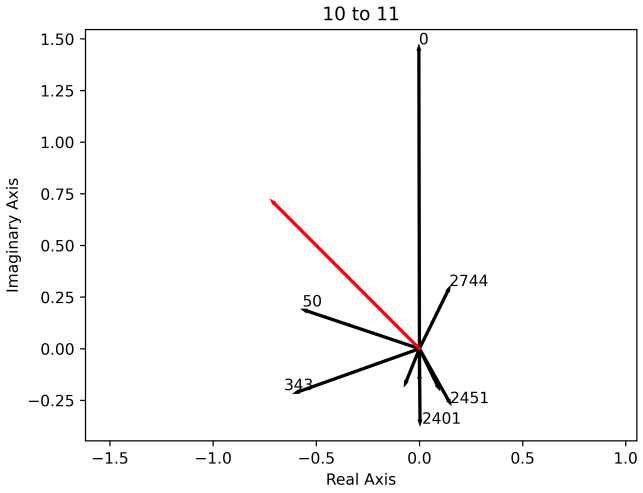

FIG. 6: The non-Hermitian pathway class amplitudes of the first CNOT gate for pathways from $|10\rangle$ to $|11\rangle$. Each amplitude is drawn as an arrow and pathway classes with large enough magnitudes are labeled with an associated frequency. The red arrow is the sum of all pathway class amplitudes and has a magnitude equal to 1. These non-Hermitian pathway classes are expanded in Table III.

this second pulse is any different from the first. Although new states show up in the population plots, it is possible that these states only appear in pathways with backtracking and did not happen to destructively cancel as in the last analysis. To answer, this question Hermitian Hamiltonian encoding was performed on both systems to give Hermitian pathway classes and their corresponding amplitudes. Hermitian pathway classes ignore any backtracking information and are therefore ideal for determining if these two CNOT gates are fundamentally different. The results of the Hamiltonian encoding for both gates are given in Tables IV and V.

As can be seen in the tables, in either starting state with either control pulse, there is one Hermitian pathway class with a significantly larger amplitude than the others. In the non-Hermitian analysis performed in the previous section all the pathways depicted in Tables II and III were members of the $[00 \to 00]^{\mathrm{H}}$ and $[10 \to 11]^{\mathrm{H}}$ pathway classes respectively. In this regard, the two control pulses have a fairly similar mechanism, with most pathways being variations of $00 \to 00$ and $10 \to 11$ with backtracking added.

Important differences in the mechanism between the two pulses arise when investigating the non-dominate Hermitian pathway classes. For the $00 \to 00$ case, the pathways classes that are being looked at are $[00 \to 01 \to 11 \to 10 \to 00]^{\mathrm{H}}$ and $[00 \to 10 \to 11 \to 01 \to 00]^{\mathrm{H}}$. In the 1st CNOT gate, these pathways had a very small role. The $[00 \to 00]^{\mathrm{H}}$ pathway class already had 99.97% the magnitude of the total sum. However, in the second CNOT gate, the magnitudes of $[00 \to 01 \to 11 \to 10 \to 00]^{\mathrm{H}}$ and

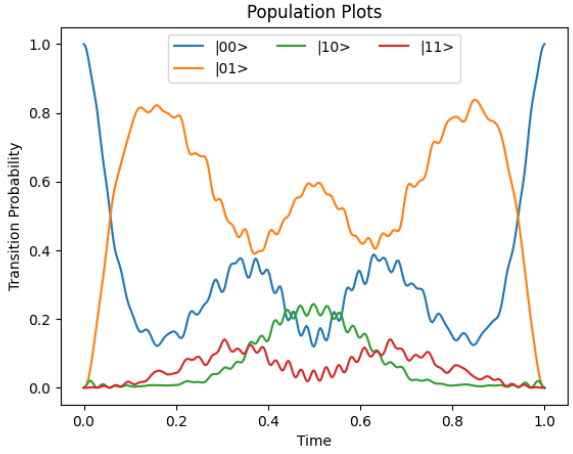

FIG. 7: Populations of all four computational basis states described by Eqs. 17 and 18 under the effect of the second CNOT gate acting on $|00\rangle$.

$[00 \to 10 \to 11 \to 01 \to 00]^{\mathrm{H}}$ are more than 15 times larger. A similar scenario occurs form the $|10\rangle$ to $|11\rangle$ pathway classes in Table V. The significance of these more complicated pathway classes signifies that the mechanism of the second CNOT gate is fundamentally different. The second CNOT gate is not the first with different backtracking, instead, it utilizes fundamentally new routes and pathways to reach the target states.

These ideas can extend more generally to other gates. They are not black boxes and different control fields can

Hermitian Pathway Class	1st CNOT Gate Magnitude	1st CNOT Gate Phase	2st CNOT Gate Magnitude	2st CNOT Gate Phase
$[00\rightarrow 00]^{\mathrm{H}}$	0.9997	136.1	0.934	154.2
$[00\rightarrow 01\rightarrow 11\rightarrow 10\rightarrow 00]^{\mathrm{H}}$	0.0093	46.9	0.163	69.6
$[00\rightarrow 10\rightarrow 11\rightarrow 01\rightarrow 00]^{\mathrm{H}}$	0.0093	46.8	0.162	65.9
...	...	...	...	...
Sum	1.000	135.0	1.000	135.0

TABLE IV: Hermitian pathway classes, amplitude magnitudes, and amplitude phases (in degrees) of both CNOT gates driving the system from $|00\rangle$ to $|00\rangle$. All pathway classes with a magnitude greater than 0.001 are listed.

Hermitian Pathway Class	1st CNOT Gate Magnitude	1st CNOT Gate Phase	2st CNOT Gate Magnitude	2st CNOT Gate Phase
$[10\rightarrow 11]^{\mathrm{H}}$	0.9997	134.4	0.951	120.8
$[10\rightarrow 00\rightarrow 01\rightarrow 11]^{\mathrm{H}}$	0.0059	-170.8	0.129	-152.3
$[10\rightarrow 11\rightarrow 01\rightarrow 00\rightarrow 10\rightarrow 11]^{\mathrm{H}}$	0.0058	-102.6	0.118	-157.0
...	...	...	...	...
Sum	1.000	135.0	1.000	135.0

TABLE V: Hermitian pathway classes, amplitude magnitudes, and amplitude phases (in degrees) of both CNOT gates driving the system from $|10\rangle$ to $|11\rangle$. All pathway classes with a magnitude greater than 0.001 are listed.

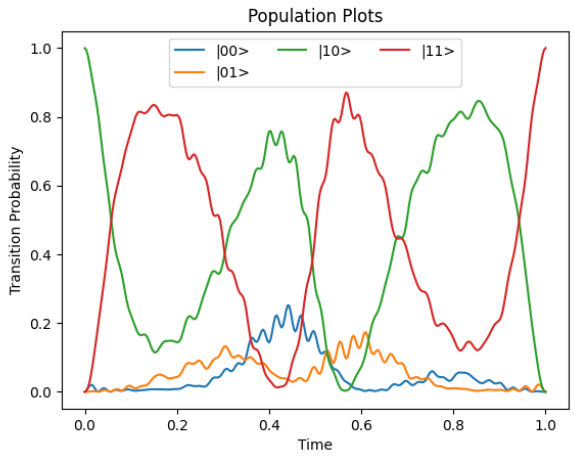

FIG. 8: Populations of all four computational basis states described by Eqs. 17 and 18 under the effect of the second CNOT gate acting on $|10\rangle$.

have different fundamental quantum dynamical mechanisms. Although two control pulses might look different, under the hood they could have very similar mechanisms and properties. These similar or different mechanisms can give rise to important properties one might want like efficiency or robustness to noise.

C. SWAP Gate

The final gate that will be investigated is the SWAP gate. The Hamiltonian for this system is the same as the previous CNOT gates described by Eqs. 17 and 18. The only difference is that the control fields $\epsilon_x(t)$ and $\epsilon_y(t)$ are chosen to implement a SWAP gate

$$\mathrm{SWAP} = \begin{pmatrix} 1 & 0 & 0 & 0 \\ 0 & 0 & 1 & 0 \\ 0 & 1 & 0 & 0 \\ 0 & 0 & 0 & 1 \end{pmatrix}. \tag{19}$$

The encoding and computation of pathways are done in the same manner as in the CNOT gates as well. This section will specifically focus on the system starting in the $|01\rangle$ state as the SWAP gate brings it to $|10\rangle$. Notice that the control Hamiltonian in Eq. 18 has no direct transition from $|01\rangle$ to $|10\rangle$, i.e. $\langle 10|H_c(t)|01\rangle = 0$. Therefore the simplest pathways connecting the states $|01\rangle$ and $|10\rangle$ will be $01\rightarrow 00\rightarrow 10$ and $01\rightarrow 11\rightarrow 10$ using $|00\rangle$ and $|11\rangle$ as intermediate states. The usage of these pathways is reflected in the population plots in Figure 9, where all four states are present during the evolution.

Mechanism analysis can be used to confirm these predictions. This is an ideal use case of Hermitian pathway classes. We want to know if the $01\rightarrow 00\rightarrow 10$ and $01\rightarrow 11\rightarrow 10$ pathways are being used disregarding potential backtracking or Rabi flopping. Hermitian encoding was performed to reveal Hermitian pathway class amplitudes which are listed in Table VI. Naturally, the two post significant pathway classes were $[01\rightarrow 00\rightarrow 10]^{\mathrm{H}}$ and $[01\rightarrow 11\rightarrow 10]^{\mathrm{H}}$. These two pathways are depicted as complex arrows in Figure 10. There were other Hermitian pathway classes but their magnitudes are comparably small and insignificant to the overall mechanism.

Here, a question can be asked: why does the $[01\rightarrow 00\rightarrow 10]^{H}$ pathway class have a 20% larger magnitude than the $[01\rightarrow 11\rightarrow 10]^{H}$ pathway class? Or in other words,

$\gamma_{ba}^{n(l_1,\ldots,l_{n-1})}/\gamma_0$	Hermitian Pathway Class	Magnitude	Phase
1	$[01\to00\to10]^{\mathrm{H}}$	0.612	50.0
0	$[01\to11\to10]^{\mathrm{H}}$	0.387	29.2
-1	$[01\to11\to10\to00\to01\to11\to10]^{\mathrm{H}}$	0.053	139.5
2	$[01\to00\to10\to11\to01\to00\to10]^{\mathrm{H}}$	0.022	44.9
...		...	...
Sum		1.000	45.0

TABLE VI: Frequencies, Hermitian pathway classes, amplitude magnitudes, and amplitude phases (in degrees) of the SWAP gate driving the system from $|01\rangle$ to $|10\rangle$. All pathway classes with a magnitude greater than 0.01 are listed.

FIG. 9: Populations of all four computational basis states described by Eqs. 17 and 18 under the effect of the SWAP gate acting on $|01\rangle$.

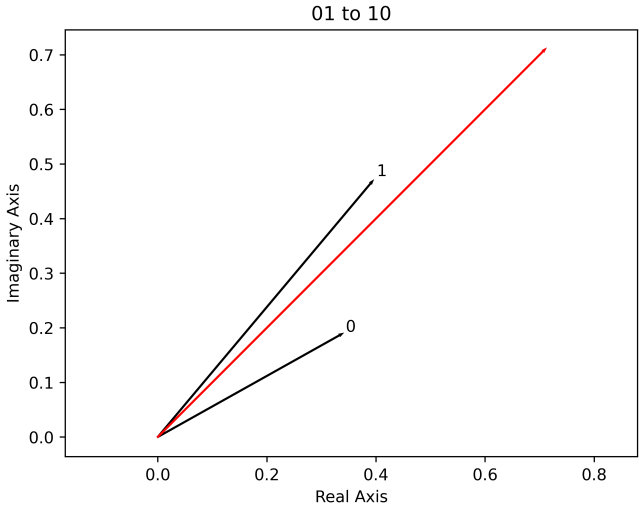

FIG. 10: The Hermitian pathway class amplitudes of the SWAP gate for pathways from $|01\rangle$ to $|10\rangle$. Each amplitude is drawn as an arrow and pathway classes with large enough magnitudes are labeled with an associated frequency. The red arrow is the sum of all pathway class amplitudes and has a magnitude equal to 1. These Hermitian pathway classes are expanded in Table VI.

why did the control decide to utilize the $|00\rangle$ state as an intermediate more than the $|11\rangle$ state? This question can be answered by looking more in-depth as the mechanism using non-Hermitian pathway classes that include backtracking information.

In Figure 11, the results of a non-Hermitian Hamiltonian encoding are presented as a complex arrow plot. However, additionally, non-Hermitian pathways classes belonging to $[01\to00\to10]^H$ are colored in blue while non-Hermitian pathways classes belonging to $[01\to11\to10]^H$ are colored in red. This colorization makes it easy to see the constructive and destructive interferences between pathway classes. Many of the most significant non-Hermitian pathways can be seen to belong to the $[01\to00\to10]^H$ pathway class. Of the seven largest pathways labeled with frequencies, six belong to $[01\to00\to10]^H$. The presence of large pathways within the $[01\to00\to10]^H$ means that the many other blue pathway classes with smaller magnitudes do not play as important roles in the mechanism. This is in contrast to the $[01\to11\to10]^H$ pathway class where there is only one pathway that is significantly larger than the rest (frequency 2401). This means that the destructive interference between the many small magnitude pathways is a significant part of the mechanism for the $[01\to11\to10]^H$ pathway class. This explains why the $[01\to00\to10]^H$ pathway class was used more by the system: because the non-Hermitian constituents of $[01\to00\to10]^H$ more efficiently use interference between pathway amplitudes.

IV. CONCLUSION

Quantum pathways and Hamiltonian encodings are powerful techniques for better understanding the mechanism behind quantum dynamical operations. The original work has been applied to many situations but this paper serves to use it on one and two qubit gates that are common in the quantum information sciences. Although the Hamiltonians being worked with were fairly general,

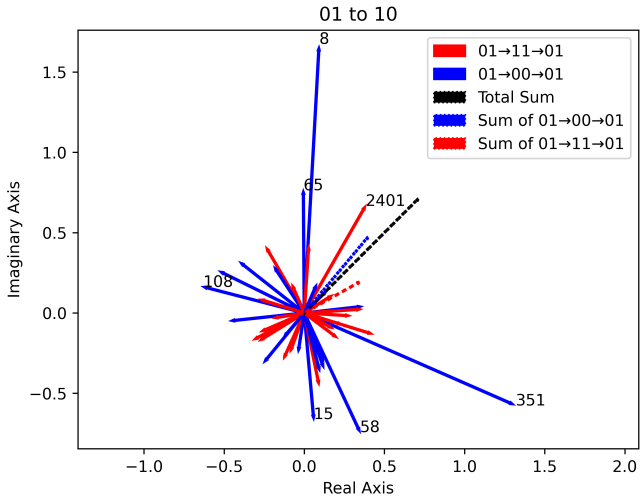

FIG. 11: The non-Hermitian pathway class amplitudes of the SWAP gate for pathways from $|01\rangle$ to $|10\rangle$. Each amplitude is drawn as an arrow and pathway classes with large enough magnitudes are labeled with an associated frequency. The solid blue pathway classes belong to the $[01\rightarrow 00\rightarrow 10]^H$ pathway class. The solid red pathway classes belong to the $[01\rightarrow 11\rightarrow 10]^H$ pathway class. The dashed blue and red pathways are the pathway amplitudes corresponding to $[01\rightarrow 00\rightarrow 10]^H$ and $[01\rightarrow 11\rightarrow 10]^H$ respectively. The dashed black arrow is the sum of all pathway class amplitudes and has a magnitude equal to 1.

these techniques can also be used on alternative qubit models with different physical implementations. In this paper, control fields for an X-gate, two CNOT gates, and a SWAP gate were investigated and interesting properties about the time evolution were explained using quantum pathways and Hamiltonian encoding. Repeating themes in the analysis were the importance of constructive/destructive interference and information about the dynamics that would otherwise be hidden from physical measurement.

The basis set out in this paper lends itself to several potential future interactions. First, this technique can instead consider noisy quantum systems with either uncertainty in the control or knowledge of the Hamiltonian. Quantum pathways may help better understand how noise affects the fidelity of a control pulse. With this knowledge, it is also possible that mechanism analysis can be used in the design of optimal controls to mitigate the effects of noise. In the same vein, this can be used to study open quantum systems to study the effect of the environment on pathways. This method requires a redefinition of the pathways to use the Lindbladian as was done in [33]. Finally, the analysis performed in the paper was only on single and two-qubit systems. In reality, a practical quantum computer needs many qubits, and pathway analysis can be performed on these much larger scales. This, however, becomes very computationally expensive as the number of qubits increases. Future work will directly explore some of these applications.

ACKNOWLEDGMENTS

The authors acknowledge support from the Department of Energy.

[1] C. D. Bruzewicz, J. Chiaverini, R. McConnell, and J. M. Sage, Trapped-ion quantum computing: Progress and challenges, Applied Physics Reviews **6**, 021314 (2019), https://pubs.aip.org/aip/apr/article-pdf/doi/10.1063/1.5088164/14577412/021314_1_online.pdf.
[2] D. Loss and D. P. DiVincenzo, Quantum computation with quantum dots, Phys. Rev. A **57**, 120 (1998).
[3] P. Kok, W. J. Munro, K. Nemoto, T. C. Ralph, J. P. Dowling, and G. J. Milburn, Linear optical quantum computing with photonic qubits, Rev. Mod. Phys. **79**, 135 (2007).
[4] M. Saffman, T. G. Walker, and K. Mølmer, Quantum information with rydberg atoms, Rev. Mod. Phys. **82**, 2313 (2010).
[5] F. Jelezko, T. Gaebel, I. Popa, M. Domhan, A. Gruber, and J. Wrachtrup, Observation of coherent oscillation of a single nuclear spin and realization of a two-qubit conditional quantum gate, Phys. Rev. Lett. **93**, 130501 (2004).
[6] M. H. Devoret and R. J. Schoelkopf, Superconducting circuits for quantum information: An outlook, Science **339**, 1169 (2013), https://www.science.org/doi/pdf/10.1126/science.1231930.
[7] W. Y. Ren-Bao Liu and L. Sham, Quantum computing by optical control of electron spins, Advances in Physics **59**, 703 (2010), https://doi.org/10.1080/00018732.2010.505452.
[8] M. J. Calderón, A. Saraiva, B. Koiller, and S. Das Sarma, Quantum control and manipulation of donor electrons in Si-based quantum computing, Journal of Applied Physics **105**, 122410 (2009), https://pubs.aip.org/aip/jap/article-pdf/doi/10.1063/1.3124084/13906141/122410_1_online.pdf.
[9] L. M. K. Vandersypen and I. L. Chuang, Nmr techniques for quantum control and computation, Rev. Mod. Phys. **76**, 1037 (2005).
[10] S. Shi and H. Rabitz, Quantum mechanical optimal control of physical observables in microsystems, The Journal of Chemical Physics **92**, https://doi.org/10.1063/1.458438 (1990).
[11] T. Cheng and A. Brown, Pulse shaping for optimal control of molecular processes, The Journal of Chemical Physics **124**, https://doi.org/10.1063/1.2187977 (2006).
[12] G. A. Worth and G. W. Richings, Optimal control by computer, Annu. Rep. Prog. Chem., Sect. C: Phys. Chem. **109**, 113 (2013).
[13] A. Rothman, T.-S. Ho, and H. Rabitz, Observable-

preserving control of quantum dynamics over a family of related systems, Phys. Rev. A **72**, 023416 (2005).
[14] C.-C. Shu, T.-S. Ho, X. Xing, and H. Rabitz, Frequency domain quantum optimal control under multiple constraints, Phys. Rev. A **93**, 033417 (2016).
[15] C. P. Koch, M. Lemeshko, and D. Sugny, Quantum control of molecular rotation, Rev. Mod. Phys. **91**, 035005 (2019).
[16] R. Chakrabarti and H. Rabitz, Quantum control landscapes, International Reviews in Physical Chemistry **26**, 671 (2007), https://doi.org/10.1080/01442350701633300.
[17] P. Doria, T. Calarco, and S. Montangero, Optimal control technique for many-body quantum dynamics, Phys. Rev. Lett. **106**, 190501 (2011).
[18] P. Rembold, N. Oshnik, M. M. Müller, S. Montangero, T. Calarco, and E. Neu, Introduction to quantum optimal control for quantum sensing with nitrogen-vacancy centers in diamond, AVS Quantum Science **2**, 024701 (2020).
[19] L. Greenman, K. B. Whaley, D. J. Haxton, and C. W. McCurdy, Optimized pulses for raman excitation through the continuum: Verification using the multiconfigurational time-dependent hartree-fock method, Phys. Rev. A **96**, 013411 (2017).
[20] M. Rossi, D. Mason, J. Chen, Y. Tsaturyan, and A. Schliesser, Measurement-based quantum control of mechanical motion, Nature **563**, 53 (2018).
[21] A. Soare, H. Ball, D. Hayes, J. Sastrawan, M. Jarratt, J. McLoughlin, X. Zhen, T. Green, and M. Biercuk, Experimental noise filtering by quantum control, Nature Physics **10**, 825 (2014).
[22] D. Press, T. D. Ladd, B. Zhang, and Y. Yamamoto, Complete quantum control of a single quantum dot spin using ultrafast optical pulses, Nature **456**, 218 (2008).
[23] R. L. Kosut, G. Bhole, and H. Rabitz, Robust quantum control: Analysis & synthesis via averaging, arXiv preprint arXiv:2208.14193 (2022).
[24] A. Koswara, V. Bhutoria, and R. Chakrabarti, Robust control of quantum dynamics under input and parameter uncertainty, Phys. Rev. A **104**, 053118 (2021).
[25] D. Daems, A. Ruschhaupt, D. Sugny, and S. Guerin, Robust quantum control by a single-shot shaped pulse, Physical Review Letters **111**, 050404 (2013).
[26] G. Dridi, K. Liu, and S. Guérin, Optimal robust quantum control by inverse geometric optimization, Physical Review Letters **125**, 250403 (2020).
[27] X. Ge, H. Ding, H. Rabitz, and R.-B. Wu, Robust quantum control in games: An adversarial learning approach, Physical Review A **101**, 052317 (2020).
[28] A. Mitra and H. Rabitz, Identifying mechanisms in the control of quantum dynamics through hamiltonian encoding, Phys. Rev. A **67**, 033407 (2003).
[29] E. Abrams, M. Kasprzak, G. Bhole, T.-S. Ho, and H. Rabitz, Efficient hamiltonian encoding algorithms for extracting quantum control mechanism as interfering pathway amplitudes in the dyson series (unpublished).
[30] A. Mitra, I. R. Solá, and H. Rabitz, Revealing quantum-control mechanisms through hamiltonian encoding in different representations, Phys. Rev. A **67**, 043409 (2003).
[31] A. Mitra and H. Rabitz, Quantum control mechanism analysis through field based hamiltonian encoding, The Journal of Chemical Physics **125**, 194107 (2006), https://doi.org/10.1063/1.2371079.
[32] R. Sharp, A. Mitra, and H. Rabitz, Principles for determining mechanistic pathways from observable quantum control data, Journal of Mathematical Chemistry **44**, 142 (2008).
[33] F. Gao, R. Rey-de Castro, Y. Wang, H. Rabitz, and F. Shuang, Identifying a cooperative control mechanism between an applied field and the environment of open quantum systems, Phys. Rev. A **93**, 053407 (2016).
[34] A. Mitra and H. Rabitz, Mechanistic analysis of optimal dynamic discrimination of similar quantum systems, The Journal of Physical Chemistry A **108**, 4778 (2004).
[35] A. Mitra and H. Rabitz, Quantum control mechanism analysis through field based hamiltonian encoding: A laboratory implementable algorithm, The Journal of Chemical Physics **128**, 044112 (2008), https://doi.org/10.1063/1.2820787.
[36] R. Rey-de Castro and H. Rabitz, Laboratory implementation of quantum-control-mechanism identification through hamiltonian encoding and observable decoding, Physical Review A **81**, 063422 (2010).
[37] R. Rey-de Castro, R. Cabrera, D. I. Bondar, and H. Rabitz, Time-resolved quantum process tomography using hamiltonian-encoding and observable-decoding, New Journal of Physics **15**, https://doi.org/10.1088/1367-2630/15/2/025032 (2013).
[38] N. J. Higham, The scaling and squaring method for the matrix exponential revisited, SIAM J. Matrix Anal. Appl. **26**, 1179–1193 (2005).